Heliyon 9 (2023) e17596

Contents lists available at ScienceDirect

Heliyon

journal homepage: www.cell.com/heliyon

Epikarst water detection using integrated geophysical methods

Chengliang Du [a], Yixiang Chen [b,c,*], Hua Xie [a], Xiaohua Lai [a], Jing Lin [a]

[a] Guang Xi Polytechnic of Construction, Nanning, 530007 China
[b] Institute of Karst Geology, Chinese Academy of Geosciences, Guilin, 541004, China
[c] Karst Dynamics Laboratory, MLR and GZAR, Guilin, Guangxi 541004, China

ARTICLE INFO

Keywords:
Self-potential method
Epikarst water
Differential filtering method
Method system
Guangxi

ABSTRACT

When detecting epikarst water using the self-potential method, the actual location of the anomaly center often deviates from the prospecting result due to the interference of the regional background field, which is comprised of geological noise and artificial electromagnetic fields. Ultimately, this makes it difficult to locate the detection target accurately. To address the potential offset of the anomaly center location, in this study we introduce the differential filtering method into the data processing procedure. This method has smoothing and low-pass filtering effects, facilitating the extraction of meaningful anomalies. Meanwhile, based on the anomalous features of different physical parameters, we propose an integrated method system based on differentially filtered horizontal self-potential gradient data, the composite profile method, and the high-density electrical method, which can effectively improve the accuracy of anomaly localization. This newly established method system was applied at the Xiaguantun test site in Longzhou County, Chongzuo, Guangxi Province, China, and its effectiveness and feasibility was confirmed.

1. Introduction

In some karst areas located in Guangxi Province, China, loss of precipitation is significant due to the unique hydrogeological conditions associated with this type of landscape. The resulting shortages in water are one of the main reasons for the poverty experienced by many in these regions. Many geological studies have shown that epikarst water is generally preserved at a depth of 0–30 m in the karst regions of Guangxi. Although epikarst water occurs in the shallow subsurface, the conduits and space for groundwater storage are small, with complex distribution patterns. As a result, water stores can only be effectively explored using high-resolution prospecting methods.

The self-potential method is widely applied because of its low cost, high efficiency, and simple operation process. It also has the advantages of a high accuracy, good operability, and wide application range when detecting small-scale, non-uniform water flows. Based on the fact that self-potentials are generated when hydrodynamic conditions change during the seepage and migration of groundwater in the epikarst zone, this study focuses on applying the self-potential method to further explore the vertical migration pattern of epikarst water down to the deep aquifers. The self-potential method has been widely employed to detect the direction and rate of groundwater flow in loose aquifers. For instance, Fagerlund and Heinson [1] applied this method to measure the direction and rate of horizontal groundwater flow. Similarly, Bumpus and Kruse [2] monitored the sinkholes (sandy collapse conduits) that provide concentrated recharge to the underlying aquifers in Central West Florida, USA, using the self-potential method to evaluate the

* Corresponding author. Institute of Karst Geology, Chinese Academy of Geosciences, Guilin, 541004, China.
E-mail addresses: chldu_123@163.com (C. Du), 13807737473@163.com (Y. Chen).

https://doi.org/10.1016/j.heliyon.2023.e17596
Received 21 February 2023; Received in revised form 20 June 2023; Accepted 21 June 2023
Available online 29 June 2023

temporal variability of water flow and determine the recharge rate of an underlying aquifer through the collapse conduits. Based on the self-potential method sensitive to water fluxes in saturated and partially saturated porous media, Jougnot et al. [3] adopted a coupled hydrogeophysical modeling framework to simulate the self-potential response to precipitation and saline tracer infiltration. Chalikakis [4] overviewed the contribution of geophysical methods to karst-system exploration, particularly emphasize that a karst area remains a very difficult environment for any geophysical exploration; selection of the best-suited geophysical method is not always straightforward, due to the highly variable and unpredictable target characteristics. Simultaneously, Binley et al. [5] documented how geophysical methods have emerged as valuable tools for investigating shallow subsurface processes over the past two decades and offer a vision for future developments relevant to hydrology and also ecosystem science. Slater et al. [6] findings suggest that the estimation of contrasts in K in coarse sediments may be achievable through measurements of electrical properties after appropriate consideration of the cobble fraction. Essa and Elhussein used a new approach for the interpretation of self-potential data by 2-D inclined plate [7]. Ikard and Pease [8] identified the preferential channels of groundwater seepage in porous media from self-potential data. Thibaut et al. [9] proposed a new workflow to apply the Minimum Gradient Support (MGS) to real case studies where heterogeneous structures are expected. More recently, Hermans et al. [10] put forward 4D imaging techniques thus to advocate a more systematic characterization of the dynamic and 3D nature of the subsurface for a series of critical processes and emerging applications. Laurence Jouniaux et al. [11] wrote a review on the use of the self-potential method to address various problems in hydrogeology and contaminant plumes. Then Revil [12] made a comment on it, Affirmed its positive influence and put forward the existence of several problems. Jardani et al. [13] Detected preferential infiltration pathways in sinkholes using joint inversion of self-potential and EM-34 conductivity data. Roubinet et al. [14] present a highly efficient two-dimensional discrete-dual-porosity approach for solving the fluid flow and associated self-potential problems in fractured rock. Talking about the Theory and Applications in Environmental Geosciences, Two works must be mentioned, "The Self-Potential Method: Theory and applications in environmental geosciences." Wrote by Revil [15]and "Advances in Modeling and Interpretation in Near Surface Geophysics" Writed by Biswas [16], both of them described a large number of SP research progress and application examples.

As the self-potential anomalies of the water-rich fractures in epikarst zones are weak and superposed with electromagnetic interference, meaningful self-potential anomalies are difficult to identify. In fact, the center of the self-potential anomaly tends to deviate from the center of the actual water-bearing fracture network. Such an offset is often caused by the background field or other noise interference. Therefore, there is a need to modify the data processing method when monitoring water-bearing fractures in epikarst zones to highlight the signal-to-noise ratio and improve the detection accuracy.

As a potential field, all potential field data processing methods can be used for reference in the process of self-potential data processing. Least square method [17–23]、Particle Swarm Optimization (PSO) [24,25], Very Fast Simulated Annealing (VFSA) overall optimization algorithm [26,27] 、Potential-field separation [28] 、 field source rapid imaging method [29,30] and Bat optimizing algorithm (BOA) [31]are some common methods in the process of self-potential data processing. Potential field separation can improve the accuracy of detection, and the fast imaging method of potential field source can provide relevant information of field source. Eigenvalue point method is an important technique for potential field separation.

Eigenvalue point method is a method of constructing linear equations to deal with anomalies by using the characteristics corresponding to outliers and eigenvalues. Its application in self-potential method is studied as follows: Radhakrishna et al. [32] presented a new method of interpreting self-potential anomalies of inclined sheet-like bodies of infinite strike length in there study; Abdelrahmanet al [33] developed a semi-automatic method to determine the depth and shape (shape factor) of a buried structure from second moving average residual self-potential anomalies obtained from observed data using filters of successive window lengths; Fedi and Abbas [34] presented a fast interpretation of self-potential data using the depth from extreme points method; Revil et al. [35] used the extreme point depth (DEXP) method to rapidly interpret the self-potential data; Chenglianget al [36] separated anomalies of horizontal gradients of the self-potential field based on first-order difference.

Considering the anomalous characteristics of different geophysical parameters, the anomalies can be detected and any interference can be comprehensively removed to highlight the meaningful anomalies and improve the accuracy of anomaly localization. In this study, a geophysical method system was developed for epikarst water detection based on the low resistivity orthogonal points revealed by the composite profiling method, the closed ring-shaped or strip-like low-resistivity anomalies in the apparent resistivity profile inverted by the resistivity method, and low self-potential anomalies, supplemented by the differential filtering method for horizontal self-potential gradient data processing.

To verify the effectiveness of the proposed system, epikarst water prospecting was conducted within a typical karst depression at Xiaguantun, Longzhou County, Chongzuo in Guangxi Province, China. The prospecting results showed that this method system was effective and feasible for epikarst water detection.

2. The method

2.1. Detecting anomalous features of groundwater in epikarst fracture networks using the composite profiling method

The composite profiling method uses two sets of three-pole devices for joint profiling. Since anomalies are detected with two apparent resistivity curves, this method is sensitive to anomalies, such that the anomalies can be clearly revealed. The low resistivity orthogonal point of the composite curve appears above a good conductor, making this method an effective way to detect groundwater in fissures. The water-bearing epikarst zone has a relatively low resistivity, which can generate a clear low resistivity orthogonal point. The location of the orthogonal point usually indicates the location of groundwater storage in an epikarst zone (Fig. 1).

2.2. Detecting anomalous features of groundwater in epikarst fracture networks using the high-density electrical method

The high-density electrical method is essentially a conventional direct current method. It has the same principles as the high-density electrical method, which is based on the difference in dielectric properties. Engineering geological and hydrogeological problems are solved by monitoring and analyzing the subsurface electric current field induced by an artificial source [37,38].

Due to the wide range of the electric field generated by the three-pole device (unipolar-dipole) used in the high-density electrical method, a greater depth can be detected than other devices. Meanwhile, the three-pole device can perform the measurement in two directions with minor boundary loss (Data measured by the tripole device can form a rectangular forward and inverse graph, while data measured by other devices are mostly inverted trapezoid or inverted triangle, with incomplete boundaries), enabling more abundant data to be obtained. Given the above advantages, the three-pole device is commonly applied in epikarst water prospecting with the high-density electrical method (Fig. 2). The apparent resistivity of the three-pole device can be calculated using Eq. (2.1):

$$\rho_s = k\frac{\Delta U_{MN}}{I} \quad k = 2\pi n(n+1)a \tag{2.1}$$

where ρ_s is the apparent resistivity and k is the configuration coefficient.

When an epikarst fracture network is developed, the water-bearing fractures exhibit low-resistivity anomalies relative to the intact surrounding rock mass, while the air-filled fractures show high-resistivity anomalies relative to the intact surrounding rock mass. The epikarst water is characterized by closed ring-shaped or strip-like low-resistivity anomalies in the apparent resistivity profile inverted by the resistivity method.

2.3. Detecting anomalous features of groundwater in epikarst fracture networks using the self-potential method

Self-potential signals are generated in the epikarst zone only when there is groundwater seepage in the fracture network. Field observations have shown that even if the resistivity of groundwater in the fracture network is low, the groundwater zone is shallow, or the aquifer is thin, the self-potential data of a certain magnitude can still be generated and observed. Therefore, the self-potential method has unique advantages in detecting and identifying groundwater in the epikarst fracture network.

The self-potential signals can be measured using the self-potential method or the self-potential gradient method. The groundwater conduits in the epikarst zone of karst depressions are generally narrow and interconnected into a network, such that the spacing between adjacent measurement points is small when applying the self-potential method or the self-potential gradient method in order to increase data resolution.

As the water head pressure of groundwater seepage in the epikarst fracture network is typically low, and the seepage migration is also relatively slow, the self-potential curve over the cross-section of the water flow is similar to that over a polarized sphere. According to the analogy and similarity theories in geology, the variations of self-potential signals associated with groundwater in epikarst fracture networks with different burial depths and different flow rates and directions can be analogously analyzed by investigating the self-potential curves over the polarized spheres with different burial depths and different spherical radii. For convenience, in this study, we selected a vertically polarized sphere for the theoretical calculation. The response characteristics of the self-potential with a change in one variable were explored when the other variables were assumed to remain constant.

For the vertically polarized sphere whose center was buried at depth h (Fig. 3), the self-potential generated at point P (x,0,0) on the ground surface was calculated as follows Eq. (2.2):

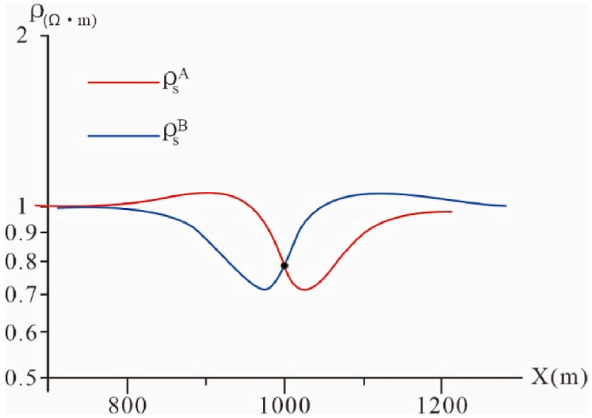

Fig. 1. Low resistance positive intersection of resistivity composite profiling method
ρ_S^A: Resistivity curve observed by the three-pole device AMN.
ρ_S^B: Resistivity curve observed by the three-pole device MNB.

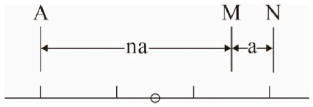

A： Source electrode. M ∝ N： Measuring electrod.

a: Electrode distance. n: Natural number.

Fig. 2. Different devices arrangement mode of the high-density electrical method
A: Source electrode. M∝*N*: Measuring electrode.
a: Electrode distance. n: Natural number.

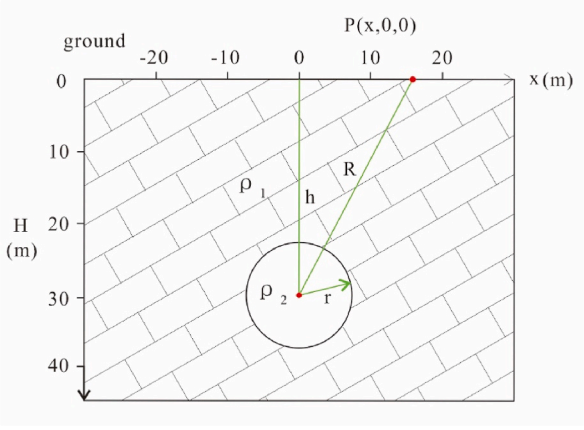

Fig. 3. Spatial position of spontaneous polarized sphere.

$$U = -\mathrm{M}\frac{h}{\left(h^2+x^2\right)^{3/2}} \tag{2.2}$$

where $\mathrm{M} = \frac{2\rho_1}{2\rho_2+\rho_1} r^2 \Delta U_0$.

ΔU_0 is the maximum value of electric potential jump on the surface of the sphere with spontaneous polarization, taken as $\Delta U_0 = 1$ (mv), r is the radius of the sphere with spontaneous polarization (m), ρ_1 is the resistivity of the surrounding rock mass, taken as $\rho_1 =$ 10,000 (Ω m), and ρ_2 is the resistivity of the karstified rock mass, taken as $\rho_2 = 1000$ (Ω m).

2.3.1. Variation of self-potential with sphere radius at a constant burial depth

The self-potential curve under varying sphere radius when the sphere center was buried at a fixed depth of $h = 30$ m and the resistivity values of the surrounding rock mass and the polarized body were $\rho_1 = 10{,}000$ Ω m and $\rho_2 = 1000$ (Ω m), respectively, is

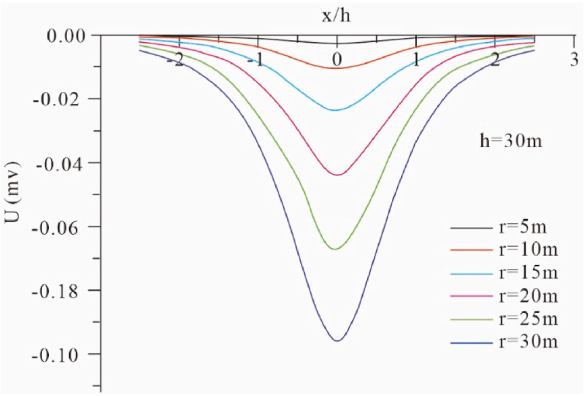

Fig. 4. SP curves for different sphere radius when sphere center depth is constant (h = 30 m).

shown in Fig. 4.

After theoretical calculation and statistical analysis, the extreme ratios of the self-potential varying with sphere radius when the burial depth of the sphere center was constant ($h = 30$ s) are listed in Table 1. In addition, the curve of the extreme ratio of the self-potential varying with sphere radius is plotted in Fig. 5, where x in x/h is the horizontal distance from the measurement point to the sphere center, and h is the burial depth of the sphere center.Where, $U_{i\ \min}$ is self-potential extremum when sphere radius r = im;

i refer to the ith measured point;

$r = 5{,}10,\ 15,\ 20{,}25{,}30$ m;

$C_{i\ \min}$ is the distance between self-potential half-extreme points 1/2Umin; half-extreme distance ratio: $A_i = \frac{C_{i\ \min}}{C_{5\ \min}}$ extreme ratio: $B_i = \frac{U_{i\ \min}}{U_{5\ \min}}$.

2.3.2. Variation of self-potential with the burial depth of the sphere center at a constant sphere radius

The self-potential curve under a changing burial depth of the sphere center when the sphere radius was constant at $r = 1$ m and the resistivity values of the surrounding rock mass and the polarized sphere were $\rho_1 = 10{,}000\ \Omega$ m and $\rho_2 = 1000\ \Omega$ m, respectively, is shown in Fig. 6, where x in x/r is the horizontal distance from the measurement point to the sphere center and h is the burial depth of the sphere center. After theoretical calculation and statistical analysis, the extreme ratios of the self-potential varying with the burial depth of the sphere center when the sphere radius is constant at $r = 1$ m are listed in Table 2. In addition, the curve of the extreme ratio of the self-potential varying with the burial depth of the sphere center is plotted in Fig. 7.

When the burial depth of the sphere is constant, the larger the sphere radius, the stronger the self-potential anomaly of the sphere, and vice versa. Under a constant burial depth of the sphere and varying sphere radius, the half-extremum distance ratio *Ai* of the self-potential is always 1 (i.e. the horizontal coordinate of the half-extremum keeps unchanged, but the intensity of the anomaly is changing). The variation of the anomaly intensity affects the accuracy of self-potential measurement and the resolution of the anomaly. When the radius of the sphere remains unchanged, the shallower the burial depth of the sphere, the stronger the self-potential anomaly of the sphere, and vice versa. As the burial depth of the sphere becomes shallower, the extreme ratio of the self-potential *Bi* gradually decreases, and the half-extremum distance ratio *Ai* gradually increases. The variation of the anomaly intensity also affects the accuracy of self-potential measurement and the resolution of the anomaly. Therefore, the resolution of the self-potential method in epikarst water detection depends on the development degree of the epikarst fracture network and the magnitude of spontaneous polarization of the karst water.

2.3.3. Variation characteristics of the self-potential signal and horizontal self-potential gradient curve under background interference

Karst conduits are important water storage spaces and groundwater migration channels. According to physical field theories, the distribution of self-potentials on a horizontal polarized, near-horizontal karst conduit is equivalent to that on an infinitely long, homogeneous, and isotropic horizontal cylinder model.

When there is no interference, the self-potential generated by a single model is the minimum above the center of the polarized body, and the horizontal self-potential gradient curve exhibits a zero-value intersection above the center of the polarized body. As shown in Fig. 8a,c, model B was used to simulate the shallow-buried, small-scale karstified rock mass, while model A was constructed to simulate the deep, large-scale regional background field. Due to the interference of the regional background field, the horizontal self-potential gradient curve generated by the assemblage of models A and B did not show a zero-value intersection at the location of the shallow-buried, small-scale polarized body B (i.e., the regional horizontal self-potential gradient anomaly overwhelmed the local anomaly, causing difficulties in determining the center location of the small-scale, polarized karstified rock mass). As the model spacing $d = nr_0$ continuously increased, the self-potential curves of models A and B were gradually separated; the two curves were completely separated once model spacing reached $d = nr_0 = 20r_0$. Therefore, when detecting the small-scale karstified rock mass B, it is necessary to separate the local horizontal self-potential gradients from the regional background field using the field separation method. Otherwise, the horizontal self-potential gradient anomaly generated by the small-scale karstified rock mass B cannot be identified (Fig. 8b).

2.3.4. Extraction of local self-potential gradient anomalies using the differential filter function

When detecting epikarst water using the self-potential method, the observed self-potential signals are usually weak. Such weak signals contain the information of the local field and the regional background field, with the local field submerged in the relatively strong regional background field. The local field is associated with the locally distributed heterogeneous geological bodies underground. It is the main object to be studied using the self-potential method. To highlight the weak local anomalies, the local horizontal self-potential gradients need to be separated from the regional background field. A detailed method for this procedure is reported in the literature Application of a mathematical method in geophysics: Separating anomalies of horizontal gradients of the self-potential field

Table 1
Variations of SP and radius when sphere center depth is constant (h = 30 m).

sphere radius r (m)		5	10	15	20	25	30
feature points Field value ratio	extreme ratio Bi	1	4	9	16	25	36
	half-extreme distance ratio Ai	1	1	1	1	1	1

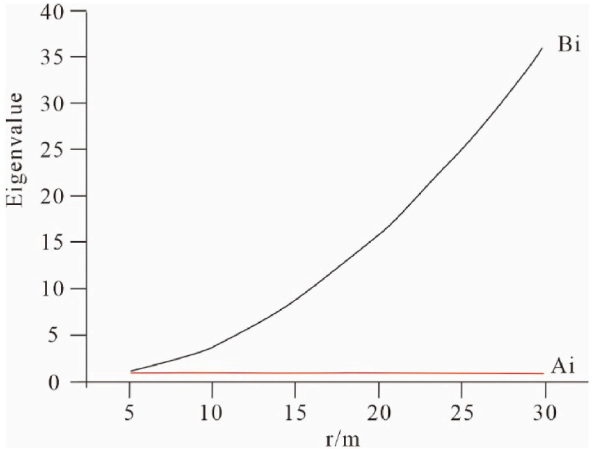

Fig. 5. Curves of self-potential's extreme ratio and half extreme distance ratio vary with sphere radius when sphere center depth is constant (h = 30 m).

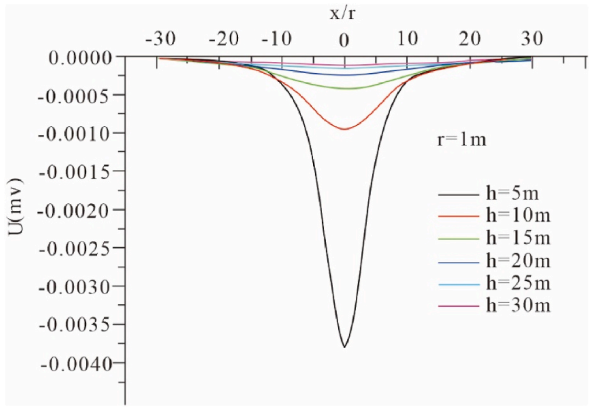

Fig. 6. SP curves for different sphere center depths when sphere radius is constant (r = 1 m).

Table 2
Self-potential's extreme ratio and half extreme distance ratio vary with sphere center depth when sphere radius is constant (r = 1 m).

burial depth h (m)		5	10	15	20	25	30
feature points Field value ratio	extreme ratio Bi	1	0.26	0.17	0.066	0.042	0.029
	half-extreme distance ratio Ai	1	2	2.6	4.4	5.5	5.7

based on first-order difference, and will be directly cited in the following.

2.4. Detecting groundwater in epikarst fracture networks using integrated geophysical methods

Our results show that the integrated geophysical methods for epikarst water detection based on the composite profiling method, resistivity method, and self-potential method, supplemented by the differential filtering method for horizontal self-potential gradient data processing, have a comprehensive theoretical basis. The procedure of epikarst water detection using integrated geophysical methods is summarized as follows.

(1) Monitor the characteristics of the self-potential curve to make preliminary judgments on the background self-potential field and the low-value anomalies; count the number of possible self-potential anomalies.
(2) Calculate the horizontal self-potential gradient and count the number of "zero-crossing points" from negative to positive horizontal self-potential gradients.

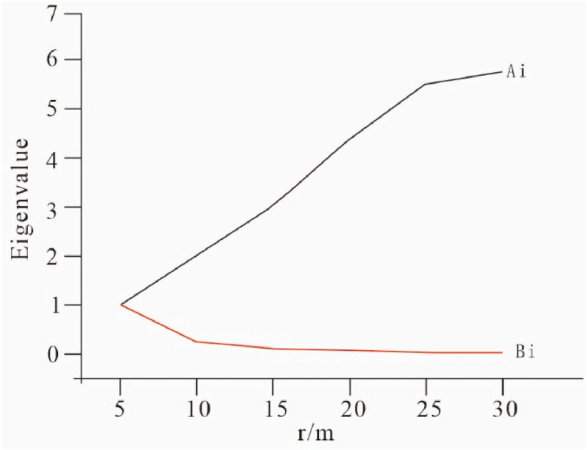

Fig. 7. Curves of self-potential's extreme ratio and half extreme distance ratio vary with sphere center depth when sphere radius is constant (r = 1 m).

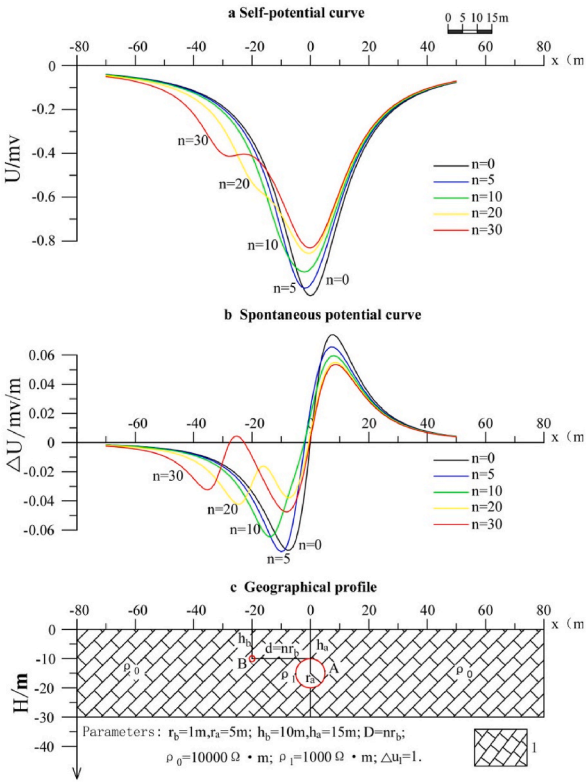

Fig. 8. SP and SP horizontal gradient curves disturbed by background field
A: Conductor in depth; B: Conductor in shallow; 3. Potential anomaly caused by conductor A;
4. Potential anomalies caused by conductor A and B; 5. Potential anomaly of horizontal gradient caused by conductor A; 6. Potential anomaly of horizontal gradient caused by conductor A and B.

(3) Perform $F\left(x_{i+1}+\frac{1}{2}\Delta x\right)$ differential filtering to the horizontal self-potential gradient curve to obtain the background field and extract the local horizontal self-potential gradient anomalies from the background field; statistically analyze the type and number of local horizontal self-potential gradient anomalies [29].

(4) For the self-potential minima, by "zero-crossing points" from negative to positive horizontal self-potential gradients, and local low-value intervals of horizontal self-potential gradients, the interference will be eliminated and any meaningful anomalies will be identified based on the principle that the locations of the meaningful anomalies of different physical parameters are

consistent. These selected anomalies are to be sorted to prioritize the self-potential anomalies most likely caused by the water-bearing fractures in the epikarst zone.

3. Results of the epikarst water detection practice at the xiaguantun test site in Xiangshui Town, Longzhou County, Guangxi Province, China

3.1. Hydrogeological setting of the study site and survey line layout

The Xiaguantun test site is located in Mianjiang Village, Xiangshui Town, Longzhou County (Fig. 9), where is comprised of mountain peaks and valleys, with the epikarst zones located within the valleys. The local lithology is thin-layered limestone of the second member of the Triassic Beisi Formation (T_1b^2). The study site is developed with two sets of near-orthogonal regional faults, trending NE and NW, respectively. At this site, the faults were mostly filled with water-blocking calcite veins, and karst terrains were relatively developed on the outer side of the fault zone. The upper reaches of the river across the test site were mainly underground, with the middle and lower reaches consisting of alternating surface and underground river sections. Groundwater mainly occurred in the epikarst fracture network, and the groundwater storage varied greatly in different regions due to the influence of geological structures and uneven karst development. According to the geological background and actual conditions of the test site, we deployed three survey lines numbered 10, 20, and 22, with a measurement point spacing of 5 m (Fig. 9b). The study site was explored using integrated geophysical methods, including the self-potential method, composite profiling method, and resistivity method.

3.2. Application process of the epikarst water detection method system in the study site

The self-potential curve along survey line 20 at the Xiaguantun test site was sawtooth-shaped, with several obvious minimum anomalies and a gentle low-potential interval between 550 and 600 m. The minimum anomalies were distributed at 410, 420, 440, 475, 485, 505, 520, 530, 540, and 550 m, respectively (Fig. 10a). The self-potential curves across the Xiaguantun test site were characterized by complex shapes, making it extremely difficult to infer the anomalies. The composite curve of the resistivity survey showed a low resistivity orthogonal point at 525 m and synchronous low-value anomalies at 405 m and 435 m (Fig. 10b). The resistivity inversion image revealed a low-resistivity anomaly within 40 m depth between 440 and 545 m. This anomaly had a wide lateral distribution range, but did not extend downward (Fig. 10c). It was difficult to determine a suitable drilling locations based on the self-potential curves and the resistivity exploration results. For this reason, we proposed to apply the differential filtering method to highlight meaningful anomalies. First, the self-potential data were differentiated to obtain the horizontal self-potential gradient curve, and 14 "zero-crossing points" from negative to positive horizontal self-potential gradients were obtained (Fig. 11). To further eliminate the interference and highlight any meaningful anomalies, the self-potential gradient data were processed using the differential filtering method to obtain the curve of local self-potential gradient anomalies. This curve was distributed with seven anomalous sites, as shown in (Fig. 11b) and Table 3: the locally minimum self-potential gradient at 435 m (with a minimum of −0.37 mv/m), 440 m (−0.56 mv/m), 500 m (−0.68 mv/m), 505 m (−0.25 mv/m), 515 m (−0.46 mv/m), 540 m (−0.44 mv/m), and 560 m (−0.31 mv/m). According to the consistency of the locations of self-potential anomalies, horizontal self-potential gradient anomalies, and local self-potential gradient anomalies, we ultimately focused on two potentially meaningful anomalies at 440 m and 505 m (Fig. 11c). Considering that the resistivity exploration results do not suggest a good apparent resistivity anomaly at 440 m, we decided to drill a well at 505 m.

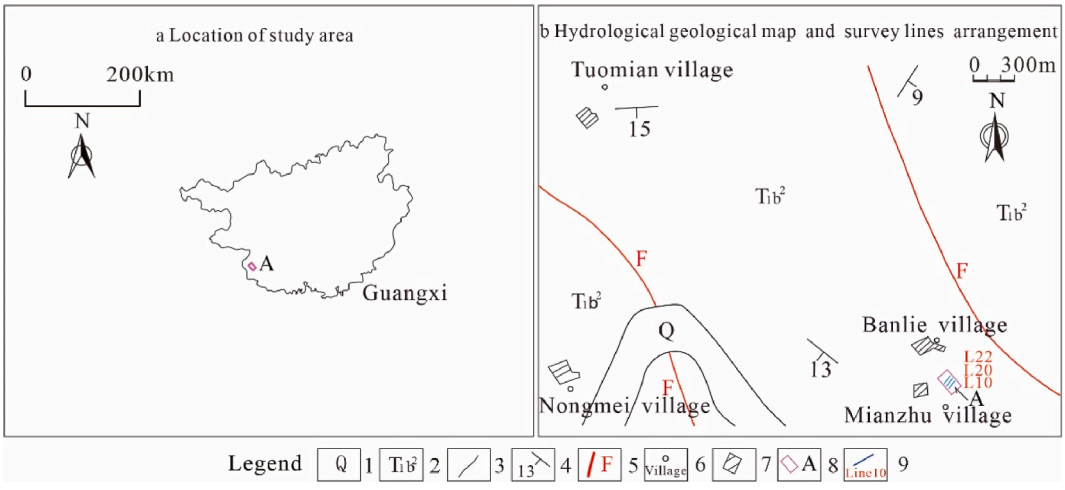

Fig. 9. Hydrological geological map of Xiaguan Village surveying area
1. Quaternary system; 2. The Member 2 of the Upper Triassic Beisi Formation; 3. Geological boundary; 4. Attitude of stratum; 5. Fault; 6. Village location and Village name; 7. Building; 8. Working Area; 9. Survey line and Line Number.

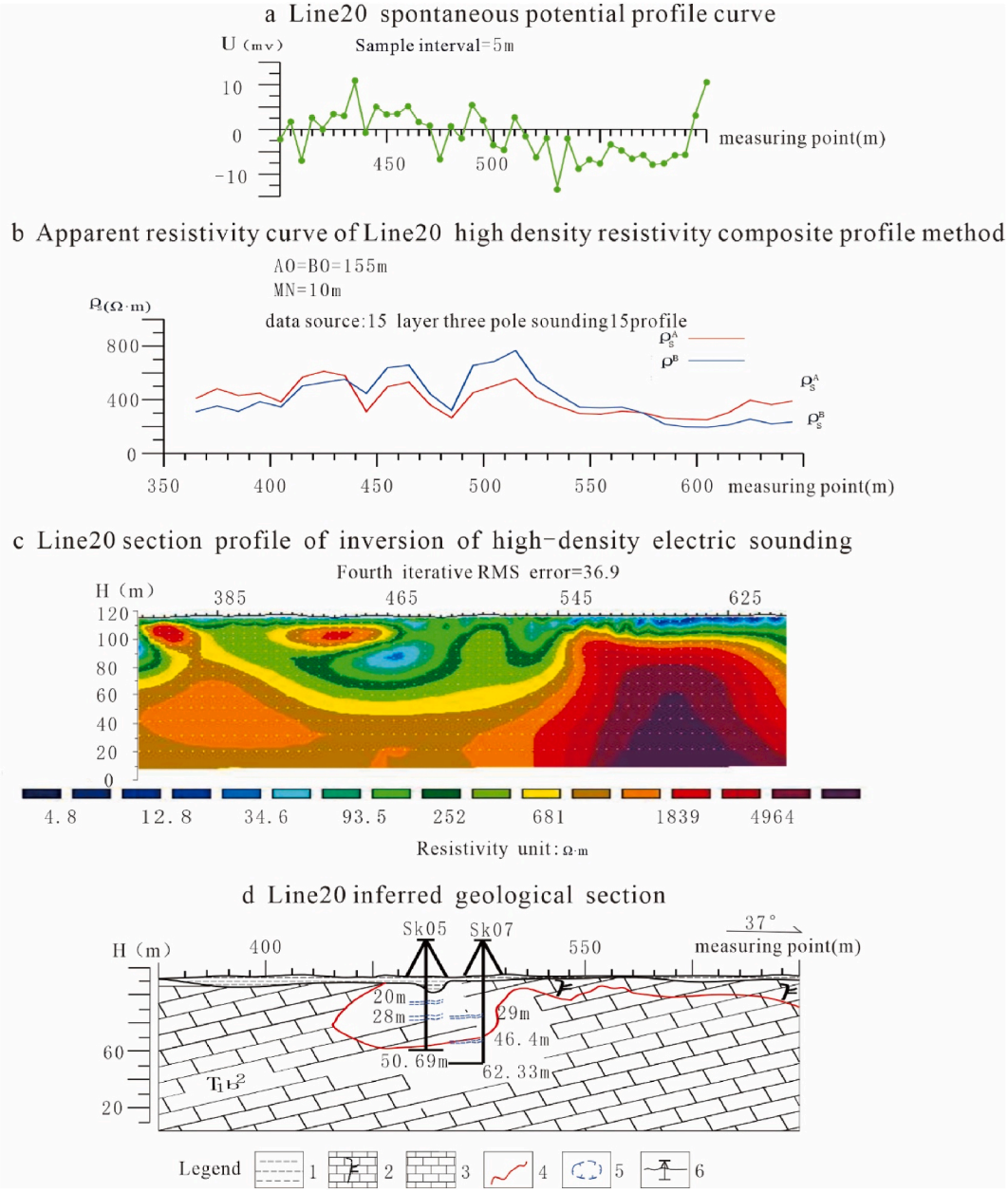

Fig. 10. Line20 integrated geophysical method detection effect profile in Xiaguan village
1. Clay; 2. Karst fissure limestone; 3. Limestone; 4. Stratigraphic boundary; 5. Karst development abnormal area; 6. Recommend drilling and geophysical exploration measuring points.

After drilling and well construction, the groundwater stored in the fracture network was found at a depth of 35.2–36.1 m and 46.4–46.7 m in well SK07, with a water yield of 60.3 m^3/d. In comparison, groundwater was not observed in the previous hydrogeological borehole ZK05 drilled at 475 m based on the resistivity exploration results (Fig. 10d).

4. Results and discussion

When detecting epikarst water using the self-potential method, due to the interference of various external factors, the measured self-potential curve is the superposition of effective local anomalies and the regional background field, so the self-potential curve exhibits a sawtooth shape. Some sawtooth-shaped anomalies are caused by external interference, while others are generated by the targeted shallow-buried water-bearing fracture network. To suppress the interference signals and highlight the meaningful anomalies, we processed the self-potential gradient data using the differential filtering method. After comprehensively analyzing the self-potential

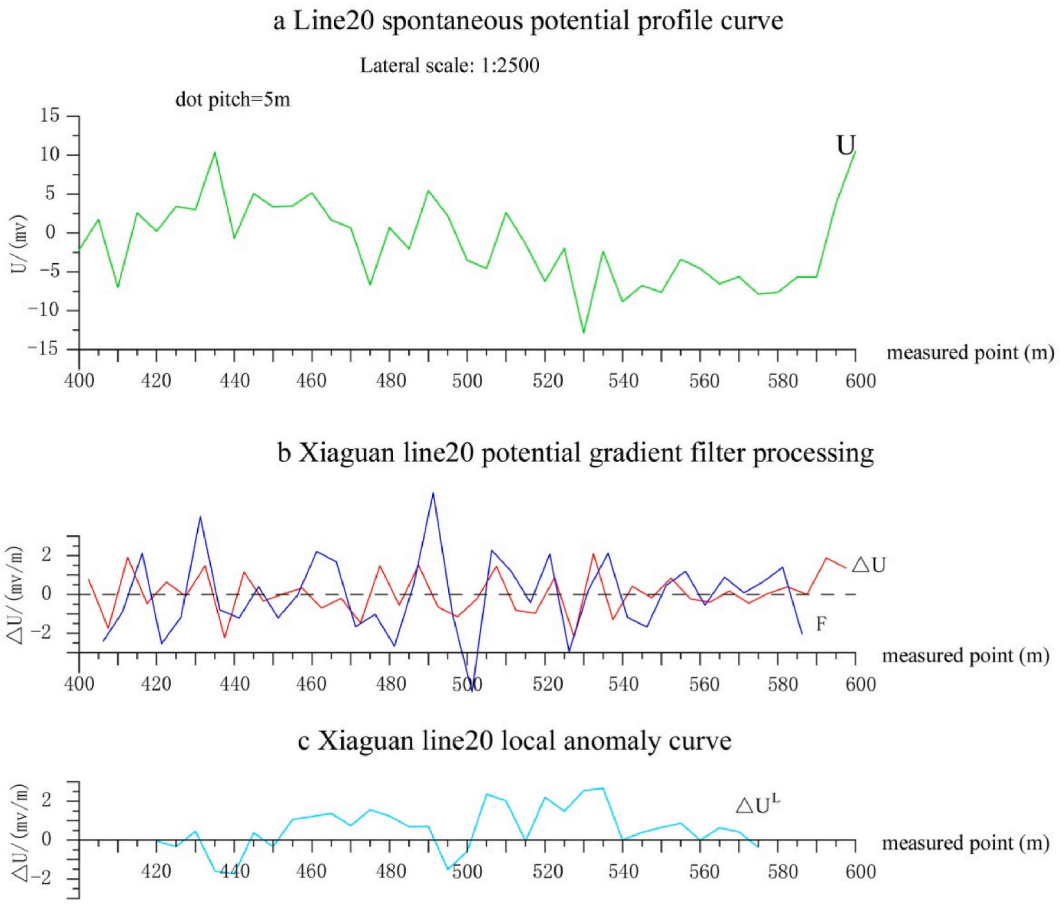

Fig. 11. Line20 detection effect profile of self-potential methods in Xiaguan.

Table 3
Statistical table of self-potential anomaly l in Xiaguan.

Physical parameters	Anomalous character	Abnormal location	Anomaly number
U	self-potential abnormal minimum value	self-potential minimum value: 10 m: 6.98mv,420 m:0.23mv, 440 m: 0.68mv,475 m: 6.67mv,485 m: 2.04mv,505 m: 4.58mv,520 m: 6.26mv,530 m: 12.68mv,540 m: 8.84mv,550 m: 7.46mv; self-potential abnormal area:550m–600 m, self-potential minimum value:585 m: 4.73mv	11
ΔU	From negative to positive "zero-crossing" anomaly	407.5 m,417.5 m,427.5 m,442.5 m,452.5 m,472.5 m,482.5 m,502.5 m,522.5 m,502.5 m,542.5 m,547.5 m,567.5 m,577.5 m	14
U^L	potential gradient local anomaly minimum value area	435 m: 0.37mv/m,440 m: 0.56mv/m,500 m: 0.68mv/m,505 m: 0.25mv/m,515 m:0.46mv/m,540 m: 0.44mv/m, 560 m: 0.31mv/m	7

anomalies, self-potential gradient anomalies, local self-potential gradient anomalies, and resistivity anomalies, the locations of meaningful anomalies can be determined based on the consistency of different types of anomalies. At the study site, according to the resistivity exploration results, low self-potential anomalies, "zero-crossing points" from negative to positive self-potential gradients, locally low self-potential gradient anomalies, and low resistivity orthogonal points anomalies were the most common anomalous features of groundwater in the epikarst zone. Eliminating the interference and identifying meaningful anomalies based on these common anomalous physical properties is an effective way to detect and identify groundwater in the epikarst fracture network.

A spherical model was used to evaluate the self-potential method for epikarst water detection. However, the actual conduits of groundwater seepage and migration in the epikarst zone are complex. More comprehensive simulation experiments from different aspects will need be conducted in the future to verify our results.

5. Conclusions

Self-potential signals are generated in the epikarst zone only when there is groundwater seepage in the fracture network. Even if the resistivity of the groundwater in the fracture network is relatively low, the groundwater zone is shallow, or the aquifer is thin, the self-potential data of a certain magnitude can still be generated and observed. Therefore, the self-potential method has unique advantages in detecting and identifying groundwater in epikarst fracture networks.

The low self-potential anomalies, "zero-crossing points" from negative to positive self-potential gradients, locally low self-potential gradient anomalies, low resistivity orthogonal points revealed by the composite profiling method and closed ring-shaped or strip-like low-resistivity anomalies in the apparent resistivity profile inverted by the high-density electrical method are the most common anomalous features of groundwater in the epikarst zone. A method system with integrated geophysical methods is established to detect groundwater in epikarst fracture networks.

The established method system for epikarst water detection was applied at the Xiaguantun test site in Xiangshui Town, Longzhou County, Guangxi Province, China. The prospecting results showed that this method system is effective and feasible for epikarst water detection. These findings serve as a reference for epikarst detection in the widely distributed karst areas in southwest China.

Author contribution statement

Chengliang Du: Conceived and designed the experiments; Performed the experiments; Analyzed and interpreted the data; Contributed reagents, materials, analysis tools or data; Wrote the paper.

Yixiang Chen: Conceived and designed the experiments; Performed the experiments; Analyzed and interpreted the data; Contributed reagents, materials, analysis tools or data.

Hua Xie: Performed the experiments.

Xiaohua Lai: Analyzed and interpreted the data.

Jing Lin: Contributed reagents, materials, analysis tools or data.

Data availability statement

Data will be made available on request.

Declaration of competing interest

The authors declare that they have no known competing financial interests or personal relationships that could have appeared to influence the work reported in this paper.

Acknowledgements

This work was supported by the National Natural Science Foundation of China (41572232). The authors thank Prof. Mark Everett, Editor-in-Chief, and the capable reviewer for their keen interest, excellent suggestions and thorough review that improved our manuscript. Also, We are grateful to Chen Yixiang at Institute of Karst Geology, Chinese Academy of Geoscience for his invaluable guide and help.

References

[1] F. Fagerlund, G. Heinson, Detecting subsurface groundwater flow in fractured rock using self-potential (SP) methods, Environ. Geol. 43 (7) (2003) 782–794.
[2] P.B. Bumpus, S.E. Kruse, Self-potential monitoring for hydrologic investigations in urban covered-karst terrain, Geophysics 79 (6) (2014) B231–B242.
[3] D. Jougnot, N. Linde, E.B. Haarder, M.C. Looms, Monitoring of saline tracer movement with vertically distributed self-potential measurements at the HOBE agricultural test site, Voulund, Denmark, J. Hydrol. 521 (2015) 314–327.
[4] K. Chalikakis, Contribution of geophysical methods to karst-system exploration: an overview, Hydrogeol. J. 19 (6) (2011).
[5] A. Binley, S.S. Hubbard, J.A. Huisman, A. Revil, D.A. Robinson, K. Singha, L.D. Slater, The emergence of hydrogeophysics for improved understanding of subsurface processes over multiple scales, Water Resour. Res. 51 (2015) 3837–3866.
[6] L. Slater, D.P. Lesmes, Electrical-hydraulic relationships observed for unconsolidated sediments in the presence of a cobble framework, Water Resour. Res. 50 (2014).
[7] K.S. Essa, M. Elhussein, A new approach for the interpretation of self-potential data by 2-D inclined plate, J. Appl. Geophys. 136 (2017) 455–461.
[8] S. Ikard, E. Pease, Preferential groundwater seepage in karst terrane inferred from geoelectric measurements, Near Surf. Geophys. 1 (17) (2019) 43–53.
[9] R. Thibaut, T. Kremer, A. Royen, B.K. Ngun, T. Hermans, A new workflow to incorporate prior information in minimum gradient support (mgs) inversion of electrical resistivity and induced polarization data, J. Appl. Geophys. 187 (2021) (2021) 1–10.
[10] H. Thomas, G. Pascal, J. Damien, H. Jan, P.B. Fleckenstein, N. Frederic, L. Niklas, A.H. Johan, B. Olivier, L.A. Jorge, H. Richard, P. Andrea, C. Anne-Karin, P. A. Álvaro, B. Lara, P. Behzad, H. Peleg, F.V. Alejandro, E.H. Guilherme, J.T.-C. Nogueira, C. Majken, Looms, K. Meruyert, D. Philippe, L.B. Tanguy, Advancing measurements and representations of subsurface heterogeneity and dynamic processes: towards 4D hydrogeology, Hydrol. Earth Syst. Sci. 1 (27) (2023) 255–287.
[11] L. Jouniaux, A. Maineult, V. Naudet, M. Pessel, P. Sailhac, Review of self-potential methods in hydrogeophysics, Compt. Rendus Geosci. 341 (10–11) (2009) 928–936.
[12] E. Auken, R. Guerin, R.D. Marsily, R. Sailhac, Comment on "review of self-potential methods in hydrogeophysics" by l. jouniaux et al. [c. r. geoscience 341 (2009) 928-936], Compt. Rendus Geosci. 342 (10) (2010) 806.
[13] A. Jardani, A. Revil, F. Santos, C. Fauchard, J.P. Dupont, Detection of preferential infiltration pathways in sinkholes using joint inversion of self-potential and em-34 conductivity data, Geophys. Prospect. 55 (5) (2007) 749–760.

[14] D. Roubinet, N. Linde, D. Jougnot, J. Irving, Streaming potential modeling in fractured rock: insights into the identification of hydraulically-active fractures, Geophys. Res. Lett. 43 (10) (2016) 4937–4944.
[15] A. Revil, A. Jardani, The Self-Potential Method: Theory and Applications in Environmental Geosciences, 2010.
[16] A. Biswas, S. Sharma, Advances in Modeling and Interpretation in Near Surface Geophysics, 2020.
[17] E.M. Abdelrahman, K.S. Essa, E.R. Abo-Ezz, K.S. Soliman, T.M. El-Araby, A least-squares depth-horizontal position curves method to interpret residual SP anomaly profiles, J. Geophys. Eng. 3 (2006) 252–259.
[18] E.M. Abdelrahman, K.S. Soliman, K.S. Essa, E.R. Abo-Ezz, T.M. El-Araby, A least-squares minimisation approach to depth determination from numerical second horizontal self-potential anomalies, Explor. Geophys. 40 (2009) 214–221.
[19] H.M. El-Araby, A new method for complete quantitative interpretation of self-potential anomalies, J. Appl. Geophys. 55 (2004) (2004) 211–224.
[20] E.M. Abdelrahman, H.S. Saber, K.S. Essa, M.A. Fouda, A least-squares approach to depth determination from numerical horizontal self-potential gradients, Pure Appl. Geophys. 161 (2004) 399–411.
[21] E.M. Abdelrahman, K.S. Essa, E.R. Abo-Ezz, M. Sultan, W.A. Sauck, A.G. Gharieb, New least-squares a logarithm for model parameters estimation using self-potential anomalies, Comput. Geosci. 34 (2008) 1569–1576.
[22] K.S. Essa, E.R. Abo-Ezz, Potential field data interpretation to detect the parameters of buried geometries by applying a nonlinear least-squares approach, Acta Geodaetica et Geophysica 56 (2021) 387–406.
[23] E.M. Abdelrahman, K.S. Essa, E.R. Abo-Ezz, K.S. Soliman, Self-potential data interpretation using standard deviations of depths computed from moving average residual anomalies, Geophys. Prospect. 54 (2006) 409–423.
[24] K.S. Essa, A particle swarm optimization method for interpreting self-potential anomalies, J. Geophys. Eng. 16 (2019) 463–477.
[25] K.S. Essa, Self potential data interpretation utilizing the particle swarm method for the finite 2D inclined dike: mineralized zones delineation, Acta Geodaetica et Geophysica 55 (2020) 203–221.
[26] A. Biswas, S. Sharma, Optimization of Self-Potential interpretation of 2-D inclined sheet-type structures based on Very Fast Simulated Annealing and analysis of ambiguity, J. Appl. Geophys. 105 (2014) 235–247.
[27] L. Xin, T. Koike, M. Pathrnathevan, A very fast simulated re-annealing (vfsa) approach for land data assimilation, Comput. Geosci. 30 (3) (2004) 239–248.
[28] S. Mehanee, K.S. Essa, P.D. Smith, A rapid technique for estimating the depth and width of a two-dimensional plate from self-potential data, Geophys. Eng. 8 (2011) 447–456.
[29] D. Patella, Introduction to ground surface self-potential tomography, Geophys. Prospect. 45 (4) (1997) 653–681.
[30] P. Mauriello, D. Patella, Gravity probability tomography: a new tool for buried mass distribution imaging, Geophys. Prospect. 49 (1) (2010) 1–12.
[31] K.S. Essa, Z.E. Diab, S.A. Mehanee, Self-potential data inversion utilizing the Bat optimizing algorithm (BOA) with various application cases, Acta Geophys. 71 (2023) 567–586.
[32] I. Murthy, K. Sudhakar, P. Rao, A new method of interpreting self-potential anomalies of two-dimensional inclined sheets, Comput. Geosci. 31 (5) (2005) 661–665.
[33] E.M. Abdelrahman, T.M. El-Araby, K.S. Essa, Shape and depth determinations from second moving average residual self-potential anomalies, J. Geophys. Eng. 6 (1) (2009) 43–52.
[34] M. Fedi, M.A. Abbas, A fast interpretation of self-potential data using the depth from extreme points method, Geophysics 78 (2013) E107–E116.
[35] A. Revil, W.F. Woodruff, C. Torres-Verdin, M. Prasad, Complex conductivity tensor of anisotropic hydrocarbon-bearing shales and mudrocks, Geophysics 78 (6) (2013) D403–D418.
[36] A. D. C, B. C. Y, A. Z. Y, A. C. B, Application of a mathematical method in geophysics: separating anomalies of horizontal gradients of the spontaneous potential field based on first-order difference - sciencedirect, J. Appl. Geophys. 176 (2020) 1–8.
[37] S. Sonkamble, V. Satishkumar, B. Amarender, Combined ground-penetrating radar (gpr) and electrical resistivity applications exploring groundwater potential zones in granitic terrain, Arabian J. Geosci. 7 (8) (2014) 3109–3117.
[38] C.L. Du, Y.S. Zhou, F.P. Gan, Y.X. Chen, Investigation of karst collapses using integrated geophysical methods: an example from conghua district, guangzhou city, China, Acta Carsol./Karsoslovni Zb. 49 (2–3) (2020) 255–264.